PHYSICAL REVIEW B **78**, 035316 (2008)

Turn-on dynamics and modulation response in semiconductor quantum dot lasers

Kathy Lüdge,[1] Moritz J. P. Bormann,[1] Ermin Malić,[1] Philipp Hövel,[1] Matthias Kuntz,[2] Dieter Bimberg,[2] Andreas Knorr,[1]
and Eckehard Schöll[1]
[1]*Institut für Theoretische Physik, Technische Universität Berlin, 10623 Berlin, Germany*
[2]*Institut für Festkörperphysik and Center of Nanophotonics, Technische Universität Berlin, 10623 Berlin, Germany*

(Received 18 January 2008; revised manuscript received 7 April 2008; published 17 July 2008; publisher error corrected 20 February 2009)

We show that the dynamic response of electrically pumped semiconductor quantum dot lasers can be quantitatively understood by including the strongly nonlinear character of electron-electron scattering processes. The numerical simulations presented here combine a microscopic approach used for calculating the nonradiative scattering rates with a rate equation model used for modeling the complex dynamic turn-on behavior. Simulated turn-on delay, relaxation oscillation frequency, small-signal modulation response, and eye patterns of the quantum dot laser are presented and compared with experimental results at an emission wavelength of 1300 nm. The strong damping of the relaxation oscillations is attributed to an anomalous mechanism which involves Auger capture, including the mixed electron-hole process from the wetting layer (WL) into quantum dot states, and relies upon the pump current dependent ratio of WL electron and hole densities.

DOI: 10.1103/PhysRevB.78.035316 PACS number(s): 42.55.Px, 42.60.Rn, 78.67.Hc

I. INTRODUCTION

Quantum dot (QD) lasers are excellent candidates for future high-speed communication and already preferential to quantum well lasers with respect to important features like threshold current, temperature stability, chirp, and feedback insensitivity.[1–3] However, cut-off frequency and data transmission rate need to be improved further in order to make them attractive for industrial applications. Therefore, there is a need to understand what limits the performance and how it can be improved. To achieve this goal, an understanding of the underlying dynamics on a microscopic level is necessary. This is the purpose of the following modeling of a directly modulated QD laser system which combines a microscopic approach for calculating the nonradiative electron-electron scattering rates with a rate equation model used for modeling the complex dynamic turn-on behavior. Thus it goes beyond standard rate equations,[4–12] which are similar to those used in quantum well lasers.[13,14] Since our focus here is not on spectrally resolved features like spectral hole burning, inhomogeneous broadening, and intradot relaxation processes, such features as included in other works[11,15–17] are neglected.

In general, a fully microscopic description of the dynamics of QD lasers above the threshold would require to describe the polarization and population dynamics of an inhomogeneous distribution of QDs in the gain regime,[18] the quantum-well wetting layer (WL), and the injection pumped bulk regions. The interaction of electrons in these states is provided by relevant relaxation processes such as electron-electron and electron-phonon interaction.[19] A fully microscopic approach for all time and length scales of the dynamics of QD lasers is by far numerically too demanding. Therefore, recent research is focused on some of the most important aspects of the QD laser dynamics: For instance, a dynamical hierarchy for the population and modulation dynamics of QD lasers in the relaxation time approximation has been outlined in Ref. 20 and a study of quantum correlations in the optical emission is provided in Ref. 21.

In our work we focus on the dynamics of relaxation oscillations on a nanosecond timescale for current injection well above the laser threshold. We focus on the population dynamics induced by the interaction of the QD states with the temporally current modulated population reservoir of wetting-layer states. In this high excitation limit, electron-electron scattering provides the main interaction channel.

A detailed comparison between experimental and theoretical data is given for a wide range of different pump currents. We achieve excellent agreement between experimentally observed and theoretically predicted dynamics resulting in the quantitative explanation of the strongly damped oscillations of the QD laser. The calculated electron-electron scattering rates show a strongly nonlinear dependence on the electron and hole densities in the wetting layer, which is found to be responsible for the strong damping of the relaxation oscillations. Furthermore we demonstrate the importance of the mixed (e-h) Auger capture processes that depend on both the electron (e) and the hole (h) density in the wetting layer. Although some insights into relaxation dynamics of the QD laser can be provided by simplified three variable systems neglecting the difference in electron and hole concentrations,[6,7,12] a more realistic model is needed in order to quantitatively reproduce and actually predict the observed dynamics. Moreover we demonstrate that two qualitatively different types of dynamic response are possible and single out the experimentally accessible parameters which determine switching between the two regimes.

The basic model used here, described by Eqs. (1)–(5) below, has already been proposed in our previous work.[22,23] Here, as an essential extension, we take into account the dependence of the carrier-carrier scattering rates on both the WL electron density and the WL hole density. We show that the ratio between these two quantities varies with the pump current. Thus, it is crucial to consider both densities separately in the model. Furthermore we discuss the influence of various parameters upon the dynamic laser output in detail and compare our simulations with experimental results. In particular, we present simulations of the turn-on characteristics, eye patterns, and small-signal modulation response.

TABLE I. Numerical parameters used in the simulation unless stated otherwise.

Symbol	Value	Symbol	Value	Symbol	Value
r_1, r_2	0.32	A	4×10^{-5} cm^2	L	1 mm
$\hbar\omega$	0.96 eV	N^{QD}	1×10^{10} cm^{-2}	a_L	15
κ	0.12ps^{-1}	N^{WL}	2×10^{13} cm^{-2}	$\varepsilon_{\mathrm{bg}}$	13.18
κ_{int}	220m^{-1}	β	5×10^{-6}	W	1.3 ns^{-1}
Γ	0.0011	γ_{xy}	3×10^{-12} cm^2	T	300 K
μ	$0.28e_0$ nm	Γ_z	2.5×10^{-3}		

II. RATE EQUATION MODEL

Our model describes a QD laser system, where the electrons are first injected into a WL before they are captured by the QDs. We consider a two-level system for electrons and holes in the QDs, since the carrier relaxation processes within the WL and within the QD states are much faster ($\sim ps$) than capture processes from the WL into the QDs at high WL carrier densities.[24] As a result, only the energetically lowest electron and hole levels in the QDs contribute crucially to the laser dynamics.[25] The following nonlinear rate equations [Eqs. (1)–(5)] for the charge-carrier densities in the QDs n_e, n_h, the carrier densities in the WL w_e, w_h, and the photon density n_{ph} determine the dynamics (e and h stand for electrons and holes, respectively):

$$\dot{n}_e = -\frac{1}{\tau_e} n_e + S_e^{\mathrm{in}} N^{\mathrm{QD}} - R_{\mathrm{ind}}(n_e,n_h) - R_{\mathrm{sp}}(n_e,n_h), \qquad (1)$$

$$\dot{n}_h = -\frac{1}{\tau_h} n_h + S_h^{\mathrm{in}} N^{\mathrm{QD}} - R_{\mathrm{ind}}(n_e,n_h) - R_{\mathrm{sp}}(n_e,n_h), \qquad (2)$$

$$\dot{w}_e = \frac{j(t)}{e_o} + \frac{n_e}{\tau_e}\frac{N^{\mathrm{WL}}}{N^{\mathrm{QD}}} - S_e^{\mathrm{in}} N^{\mathrm{WL}} - \widetilde{R}_{\mathrm{sp}}(w_e,w_h), \qquad (3)$$

$$\dot{w}_h = \frac{j(t)}{e_o} + \frac{n_h}{\tau_h}\frac{N^{\mathrm{WL}}}{N^{\mathrm{QD}}} - S_h^{\mathrm{in}} N^{\mathrm{WL}} - \widetilde{R}_{\mathrm{sp}}(w_e,w_h), \qquad (4)$$

$$\dot{n}_{\mathrm{ph}} = -2\kappa n_{\mathrm{ph}} + \Gamma R_{\mathrm{ind}}(n_e,n_h) + \beta R_{\mathrm{sp}}(n_e,n_h). \qquad (5)$$

Here $R_{\mathrm{ind}}(n_e,n_h) = WA(n_e+n_h-N^{\mathrm{QD}})n_{\mathrm{ph}}$ is the rate for the induced processes of absorption and emission, where N^{QD} denotes twice the QD density (taking into account the spin degeneracy), W is the Einstein coefficient, and A is the WL normalization area (the ridge waveguide QD laser used here has a lateral ridge dimension of $A=4\ \mu\mathrm{m}\times1$ mm). The exciton-dominated spontaneous emission in the QD is approximated by bimolecular recombination[13,26] and is modeled by $R_{\mathrm{sp}}(n_e,n_h) = (W/N^{\mathrm{QD}})n_e n_h$. The WL spontaneous recombination rate is expressed by $\widetilde{R}_{\mathrm{sp}}(w_e,w_h) = (W/N^{\mathrm{WL}})w_e w_h$ with a WL effective density of states $N^{\mathrm{WL}} = 2\times10^{13}$ cm^{-2}. Both spontaneous emission and induced processes are proportional to the Einstein coefficient[23] $w = |\mu|^2/3\acute{\nu}\varepsilon_0\hbar\left(w/c/\sqrt{\varepsilon_{\mathrm{bg}}}\right)^3$ with the dipole moment μ, the background dielectric constant $\varepsilon_{\mathrm{bg}}$, the vacuum permittivity ε_0, the speed of light c, Planck's constant $\hbar$, and frequency ω, which gives $W^{-1}=0.77$ ns.

In our approach, the carrier-light interaction is summarized in the photon density n_{ph}, which includes all longitudinal modes. The optical confinement factor Γ in Eq. (5) expresses the difference of the optical and electronic active area and is a measure for the radiative processes. According to Ref. 1 Γ depends on the QD density N^{QD}, the in-plane size of a QD γ_{xy}, the vertical confinement factor Γ_z, and the number of QD layers a_L. Including the experimental details (Table I) we obtain $\Gamma = N^{\mathrm{QD}} a_L \gamma_{\mathrm{xy}} \Gamma_z$. The spontaneous emission coefficient β stands for the probability that the photons generated during the spontaneous emission contribute to the considered laser mode in the cavity. The coefficient $\kappa = [\kappa_{\mathrm{int}} - \ln(r_1 r_2)/2L]c/\sqrt{\varepsilon_{\mathrm{bg}}}$ expresses the total cavity loss, where L is the cavity length, and r_1, r_2 are the facet reflection coefficients.[1] It is set to $\kappa=0.12$ ps^{-1} according to the experimental details given in Ref. 27 ($\kappa_{\mathrm{int}}=220$ m^{-1} are the internal losses). This value is different from Ref. 23 where a value of $\kappa=0.4$ ps^{-1} was chosen. The difference is that now the background dielectric constant of GaAs is taken into account. The carrier injection into the WL is expressed by the injection current density pulse $j(t)$ divided by the elementary charge e_0.

Another important contribution to the dynamics of QD lasers are the nonradiative carrier-carrier scattering processes. The scattering rates S_e^{in}, S_e^{out}, S_h^{in}, S_h^{out} of electrons (e) and holes (h) and scattering times $\tau_{e/h} = (S_{e/h}^{\mathrm{in}} + S_{e/h}^{\mathrm{out}})^{-1}$ are a measure for the strength of these processes. We derive these rates microscopically and analyze their dependencies upon the WL carrier densities.

III. NONLINEAR SCATTERING RATES

The description of the dynamics in InAs/GaAs QD lasers requires the inclusion of the interaction between discrete states localized at the QDs and the continuous electron and hole states at higher energies within the WL. Since we are interested in the investigation of the laser regime, i.e., the WL carrier density is very high, the capture dynamics within the QD-WL structure is dominated by Coulomb scattering (nonlocal Auger recombination).[24,28–32]

The Coulomb scattering rates for electron and hole capture from WL into QD states and vice versa are calculated microscopically as a function of the WL electron and hole density w_e and w_h. The Coulomb contributions are taken into account up to the second-order Born approximation yielding[33,34]

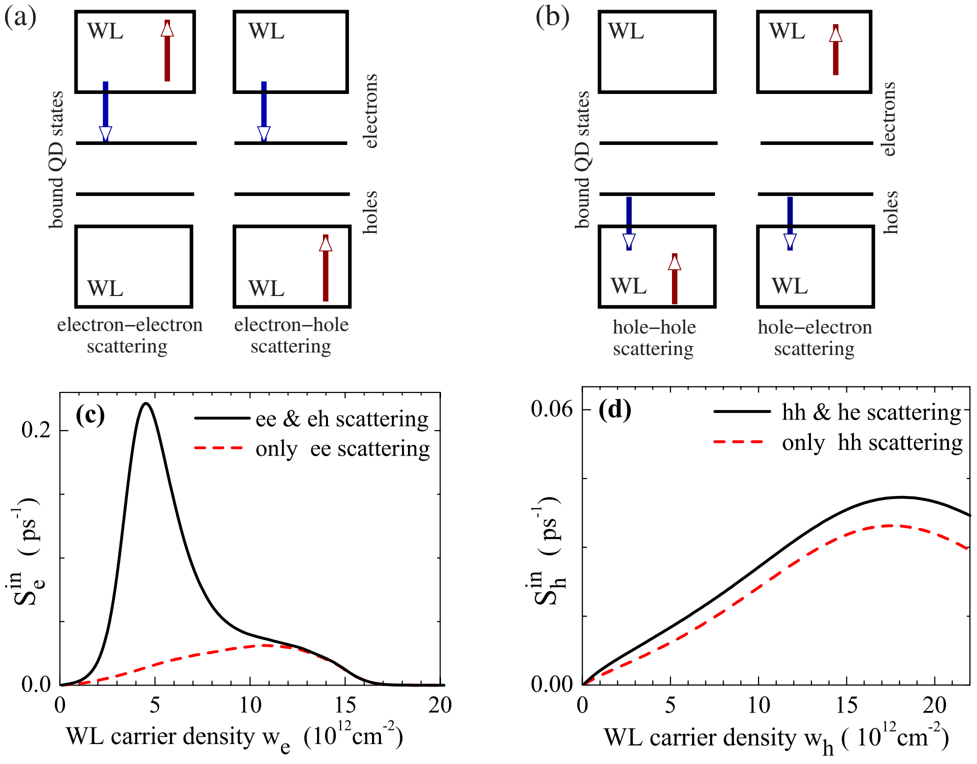

FIG. 1. (Color online) (a) Scheme of the QD-WL structure showing the Auger electron capture into a corresponding QD state (corresponding to the in-scattering rate S_h^{in}), (b) Auger hole capture into a QD state (S_h^{in}). Note that arrows denote electron transitions (inverse of the hole transitions) (c) solid (black) and dashed (red) curves display the in-scattering rate vs carrier density in the WL for electrons S_e^{in} with and without the mixed electron-hole (e,h) process, respectively; (d) same as (c) with the hole in-scattering rate S_h^{in}. For mixed processes, $w_h=3.4w_e$ is set in agreement with corresponding stationary values.

$$\dot{\rho}_b = S_b^{\text{in}}(1-\rho_b) - S_b^{\text{out}}\rho_b, \tag{6}$$

where ρ_b is the occupation probability in the electron/hole QD state ($b=e,h$). This Boltzmann-type equation contains Coulomb in- and out-scattering rates S_b^{in} and S_b^{out} with

$$S_b^{\text{in/out}} = \frac{2\pi}{\hbar}\sum_{lmnb'} M_{bnlm}(2M^*_{bnlm} - \delta_{b,b'}M^*_{bnml})f^{\text{in/out}}_{lmnb'} \times \delta(E^b + E_n^{b'} - E_l^b - E_m^{b'}). \tag{7}$$

Here, the sum runs over all WL states (occupation probabilities ρ_l^b, ρ_m^b, and ρ_n^b). The respective single-particle energies are denoted by E^b, E_l^b, $E_m^{b'}$, and $E_n^{b'}$. M_{bnlm} is the screened Coulomb matrix element. The in- and out-scattering rates are characterized by the occupation factors,

$$f^{\text{in}}_{lmnb'} = \rho_l^b\rho_m^{b'}(1-\rho_n^{b'}) \text{ and } f^{\text{out}}_{lmnb'} = \rho_n^{b'}(1-\rho_m^{b'})(1-\rho_l^b). \tag{8}$$

The microscopic approach for their calculation is described in detail in Ref. 23.

Figures 1(a) and 1(b) shows the scheme of the QD-WL structure illustrating the considered Auger capture processes for electrons and holes.[25] The energy conservation requires that the capture of an electron from a WL into a QD state is followed by either a scattering of an electron [left side of Fig. 1(a)] or a hole [right side of Fig. 1(a)] within the WL into an energetically higher state. This results in two different contributions leading to the electron capture: a pure electron-electron and a mixed electron-hole process.[35] The capture dynamics of holes is analogous [Fig. 1(b)].

The scattering rates for the mixed capture processes [electron-hole, see the right side of Fig. 1(a)] depend on both the WL carrier densities w_e and w_h. To reduce the computation time this complicated dependence is taken into account within the approximation that w_e and w_h follow a similar dynamics.[23] Then, we can assume $w_h=g_c w_e$ choosing g_c in agreement with corresponding stationary values of w_e and w_h.[23] Figure 1(c) illustrates the importance of the mixed process for the in-scattering of electrons. S_e^{in} shows a maximum followed by a shoulder at higher WL carrier densities. The latter can be ascribed to the pure electron-electron scattering, whereas the mixed scattering leads to the pronounced maximum of S_e^{in}. This is due to the higher WL hole density w_h which is responsible for the faster enhancement of the hole scattering probability within the WL. For the in-scattering dynamics of holes the mixed process contributes much less [Fig. 1(d)]. For out-scattering processes, the mixed contributions turn out to have greater influence on the height of the scattering rates but less on their qualitative shape.

Figure 2 shows the Coulomb scattering rates for electron and hole capture processes as a function of the respective WL electron and hole densities for different ratio g_c. For small w_b both the in- and out-scattering rates increase with increasing WL carrier density w_b, since there are more scattering partners available. Due to Pauli's exclusion principle the probability for out-scattering strongly decreases at high WL densities. As a result, the out-scattering rates S_b^{out} have a sharp maximum (see right column of Fig. 2. Due to the larger effective mass the population of WL states with holes proceeds more slowly than with electrons. Therefore, the effect of Pauli's exclusion principle affects the electrons faster, explaining the quicker decrease in S_e^{out}. The in-scattering rates are proportional to the product of two WL states $\rho_l^b\rho_m^{b'}$ [see Eq. (8)]. Hence, they become dominant at higher WL carrier densities at which the out-scattering is already dimin-

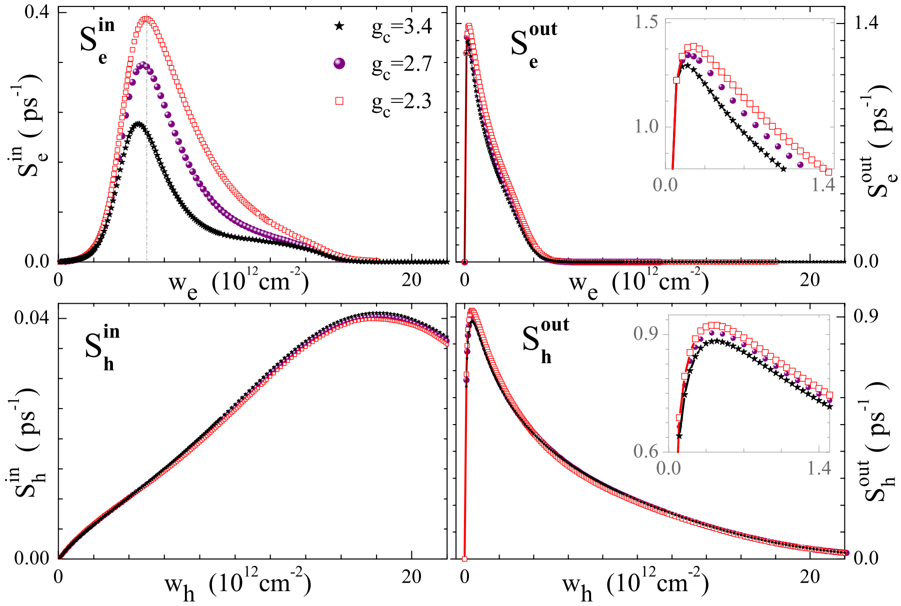

FIG. 2. (Color online) Coulomb scattering rates $S_e^{\rm in}$, $S_e^{\rm out}$, $S_h^{\rm in}$, $S_h^{\rm out}$ of electrons (e) and holes (h) vs carrier density in the WL calculated within the orthogonalized-plane-wave approach (Ref. 36) for different g_c (black stars: g_c=3.5, violet circles: g_c=2.7, and red squares: g_c=2.3). (top inset): enlargement of $S_e^{\rm out}$, (bottom inset): enlargement of $S_h^{\rm out}$.

ished by Pauli blocking (see left column of Fig. 2. Due to the faster population of electronic states $S_e^{\rm in}$ increases faster than $S_h^{\rm in}$. At very high w_b, even the in-scattering becomes weaker because the WL states are filled to a high percentage leading to a considerable decrease in the probability for the scattering processes within the WL [red arrows in Figs. 1(a) and 1(b)]. In Fig. 2 the scattering rates are plotted for different ratios between w_e and w_h, illustrating the impact of the factor g_c. As expected from the discussion above, the most drastic changes appear in $S_e^{\rm in}$ where the mixed processes contribute most.

For the simulations presented in Sec. IV, g_c is determined self-consistently for each set of parameters, e.g., after a simulation the obtained steady-state value of g_c is compared to the value assumed at the start and adjusted thereafter iteratively until it converges to a final value. Note that g_c is also a function of the pump current.

For a better comparison with simplified models one can represent the numerically evaluated scattering rates by curve-fitting functions; see the Appendix. These functions may be useful, e.g., for an approximate small-signal analysis where the Jacobian matrix of the rate equations at the steady state is needed. However, in the following sections we shall use the full nonlinear scattering rates computed numerically.

IV. TURN-ON CHARACTERISTICS

In order to discuss the results of our simulation we compare the time evolution of the simulated photon densities $n_{\rm ph}$ with experimental data from a QD laser as it is shown in Fig. 3(a). It depicts the measured laser output for different pump currents j (given in units of the laser threshold $j_{\rm th}$, which is determined from the simulated steady-state input-output characteristic $n_{\rm ph}(j)$ as shown in Fig. 4. The injection current pulse with a duration of 5 ns is switched on at t=0. The results of the simulations are shown in Fig. 3(b). For the simulation a current pulse $j(t)$=$j_0\exp[-(\frac{t-t_0}{2.5ns})^n]$ with t_0 =2.49 ns and n=90 is used, yielding a flat plateau j=j_0 and a rise and fall time of 100 ps [Fig. 5(a)]. The parameters are summarized in Table I. For a pump current of j=1.8$j_{\rm th}$ both

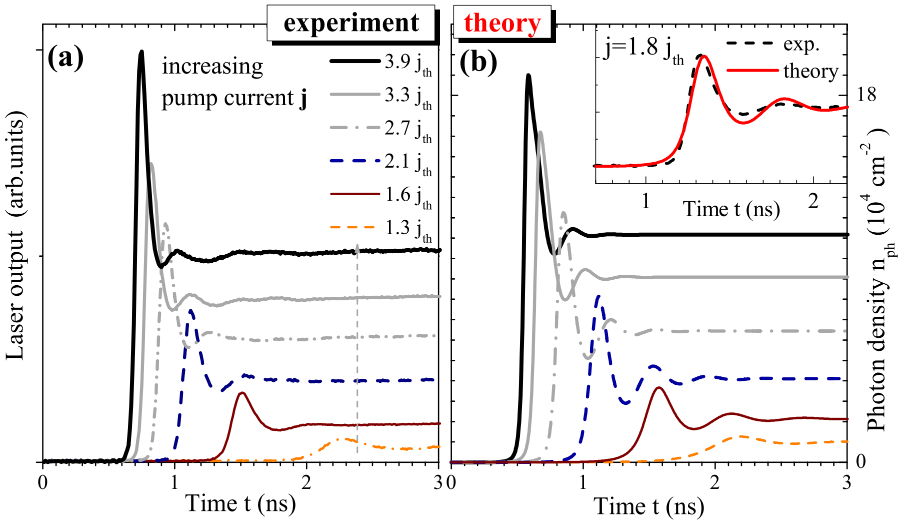

FIG. 3. (Color online) Transient turn-on dynamics: (a) measured and (b) simulated data obtained with different pump currents j (in units of $j_{\rm th}$): j =1.3$j_{\rm th}$…3.9$j_{\rm th}$. Parameters as in Table I. The inset shows experiment (black) and simulation (red) at j=1.8$j_{\rm th}$.

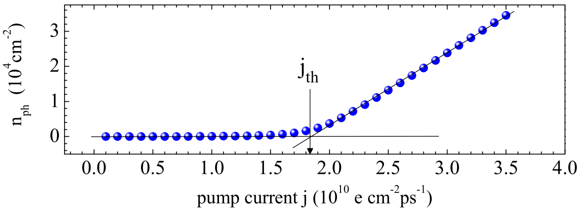

FIG. 4. (Color online) Steady-state input-output characteristic: simulated photon density n_{ph} vs injection current density j. The threshold current density j_{th}=2883A cm^{-2} is determined from the extrapolated laser onset if spontaneous emission is neglected. Parameters as in Table I.

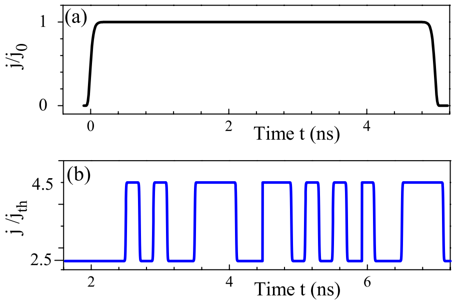

FIG. 5. (Color online) (a) Injection current pulse used in the simulations of turn-on characteristics, (b) modulated injection pulse used for eye pattern simulation (non-return-to-zero (NRZ) signal modulation).

the experimental and the simulated curves are plotted together in the inset of Fig. 3(b) to illustrate their good agreement.

A characteristic feature of QD lasers is the strongly damped relaxation oscillation showing only one pronounced peak with a full width at half maximum of Δt_{FWHM}. Also important for the laser performance is the turn-on delay time τ_{delay}, i.e., the time needed to reach the laser threshold. The frequency of the relaxation oscillations f_{RO} is also crucial as it limits the large-signal modulation response of the laser. Our simulation excellently agrees with the experimental results for all of these quantities as shown in Fig. 6. This figure separately compares the quantities f_{RO}, Δt_{FWHM}, and τ_{delay} obtained from the experimental and theoretical data of Fig. 3 over a wide range of different pump currents j. Note that j is again given in units of j_{th}. For all pump currents j the calculated relaxation oscillation frequency agrees very well with the experiment [Fig. 6(a)], displaying an approximate square root behavior. This substantially improves our previous results,[22,23] which overestimated f_{RO} by a factor of two. The reason is our more accurate treatment of the mixed (e-h) Auger process. The turn-on delay τ_{delay} and the width of the first peak of the calculated relaxation oscillations Δt_{FWHM} are also in good agreement with the experiment [Figs. 6(c) and 6(b)]. The simulation of $\tau_{delay}(j)$ shows a linear characteristic in the double logarithmic plot [Fig. 6(d)] as expected from simple rate equation models for semiconductor QW lasers[13] $\tau_{delay} \sim (j/j_{th})^{-1}$. Indeed, by similar approximations this behavior can be derived for our QD laser model: Neglecting spontaneous and induced recombination in Eqs. (1) and (3) during the transient pump process for j sufficiently far above threshold, and observing the fast transfer of electrons to QD states due to strong electron-electron scattering ($N^{QD} \ll N^{WL}$), Eq. (1) $\dot{n}_e \approx \frac{j}{e_o}\frac{N^{QD}}{N^{WL}}$ can be integrated up to threshold electron density n_{th}, which yields $\tau_{delay} \sim 1/j$. However, the experimental data show some deviations from this relation for very large and very small pump currents. This could be due to multi-transverse mode emission effects at large currents.

While the scattering rates are microscopically calculated, some parameters in the model can be chosen according to the experimental conditions. These are N^{QD}, N^{WL}, Γ, and β. In the strongly damped mode of operation the delay time τ_{delay} is essentially determined by the pump current and the Einstein coefficient W (which is included in the spontaneous and induced emission processes). W=1.3 ns^{-1} (calculated with the parameters of Table I) gives good agreement with the experiment. For larger values of W the delay time in the strongly damped regime is too small, while it is too large for smaller values of W. The optical confinement factor Γ can be varied by changing the number of QD layers a_L. We have found that the results of the simulation do not change as long as the product between Γ and the QD density N^{QD} is constant presuming that the other parameters (except β) are fixed. Using 15 layers of QDs with an in-plane size of 17 $\times$17 nm^2, Γ_z=2.5$\times$10^{-3}, and N^{QD}=1$\times$10^{10} cm^{-2}, we ob-

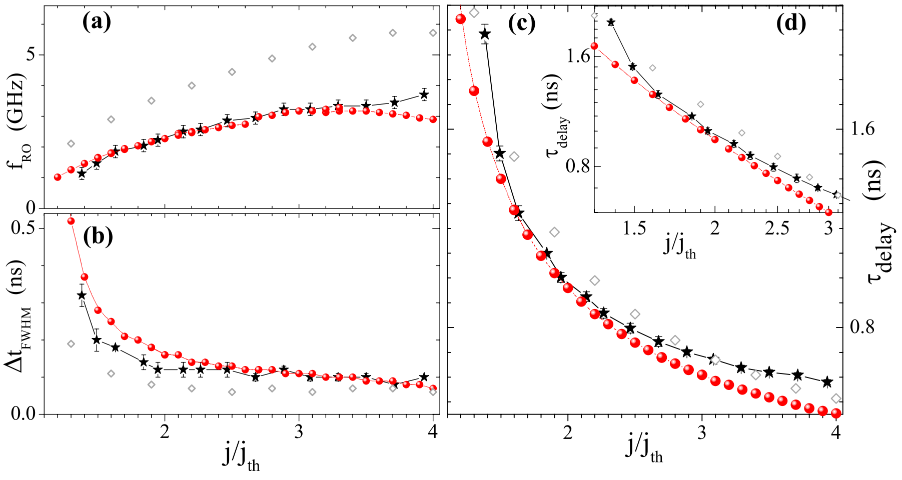

FIG. 6. (Color online) Comparison between experimental (black stars) and simulated data (red dots) plotted versus increasing pump current j/j_{th}: (a) frequency of relaxation oscillations f_{RO}, (b) the width of the first relaxation oscillation peak Δt_{FWHM}, (c) turn-on delay τ_{delay}, (d) τ_{delay} in double logarithmic plot. Parameters as in Fig. 3; open diamonds show results for different Γ =0.0015.

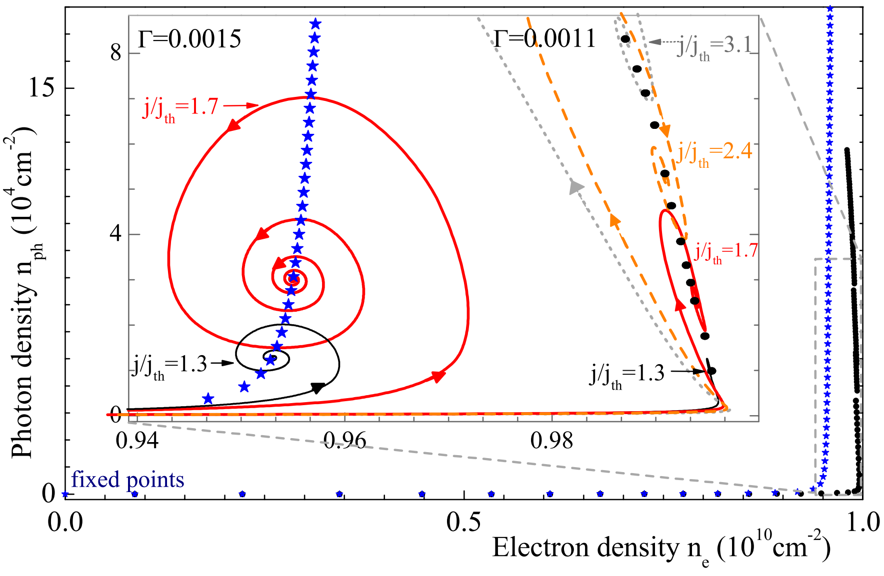

FIG. 7. (Color online) Phase portraits of photon density vs QD electron density for the weak damping ($\Gamma=0.0015$) and the strong damping ($\Gamma=0.0011$) regimes. The main picture shows the variation of the *cw* state (fixed points) with increasing pump current for two different parameter sets: Black circles correspond to $\Gamma=0.0011$; blue stars correspond to $\Gamma=0.0015$. The inset shows a blow-up of the range around the laser threshold: Relaxation oscillations are depicted as transient trajectories for different pump currents and the two values of Γ illustrating the weak and the strong damping regime, respectively (solid red lines: $j=1.7j_{th}$).

tain $\Gamma=0.0011$, which gives best agreement with the measured relaxation oscillations frequency. This value of N^{QD} is smaller than the QD density which is presumed to be present in the experimentally grown sample ($N^{QD}_{exp}=2\times10^{10}$ cm^{-2}). An explanation for this discrepancy might be that not all QDs are in resonance during the lasing process due to size fluctuations of the QDs. N^{WL} has no effect on the oscillation frequency f_{RO}. It just needs to be high enough to obtain lasing, but if it is chosen too large the scattering processes lose their influence and a strongly damped operating condition cannot be reached. N^{WL} is set to $N^{WL}=2\times10^{13}$ cm^{-2}. The spontaneous emission coefficient β controls the damping of the turn-on process. On one hand, if β is small the peak-to-valley difference of the relaxation oscillations is very large, and it decreases with increasing β. On the other hand, if β is too large only a sharp step-like turn-on behavior is found. Moreover, a change in β results in a small change in the delay time. Here, we choose $\beta=5\times10^{-6}$.

V. WEAK VERSUS STRONG DAMPING REGIME

For the electrons in the QDs there is a competition between radiative recombination and nonradiative scattering events. For stronger radiative recombination the electron-electron scattering processes lose importance, and thus the strong damping of the relaxation oscillations disappears. One parameter that affects the ratio of both processes is the optical confinement factor Γ as it is a measure for the relative importance of the radiative processes. Increasing Γ changes the dynamics completely and results in pronounced weakly damped oscillations, as shown below.

In this section we will show that by changing Γ, i.e., by varying the number of QD layers a_L, one can induce transitions between two completely different modes of laser operation: strongly damped turn-on dynamics as observed experimentally in the present sample on one hand, and slowly damped, pronounced relaxation oscillations with electron

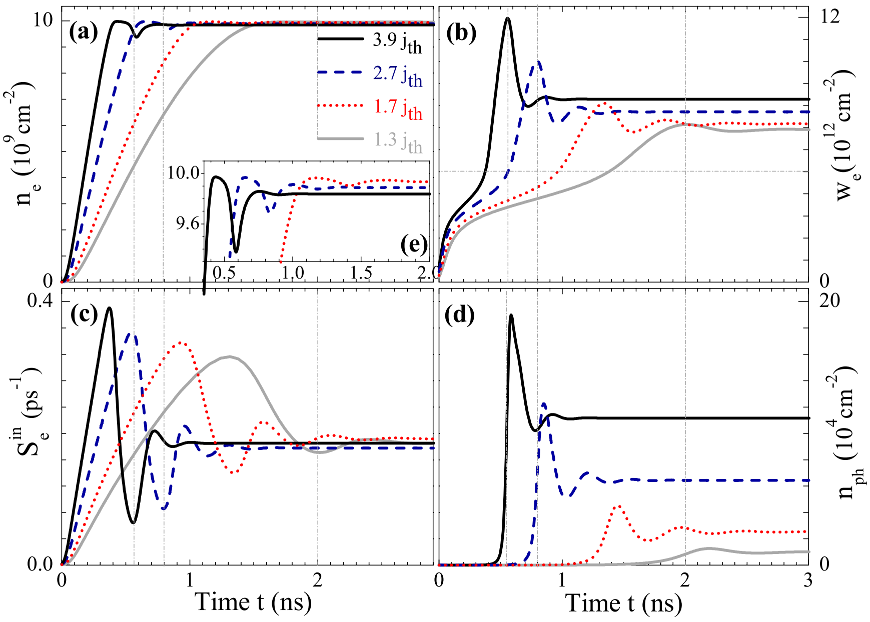

FIG. 8. (Color online) Turn-on dynamics in the strong damping regime for four different pump currents $1.3j_{th}\leq j\leq3.9j_{th}$: (a) QD electron density n_e (inset (e) shows an enlargement), (b) WL electron density w_e, (c) scattering rate for electron in-scattering S_e^{in}, and (d) photon density n_{ph}. Parameters as in Fig. 3 ($\Gamma=0.0011$).

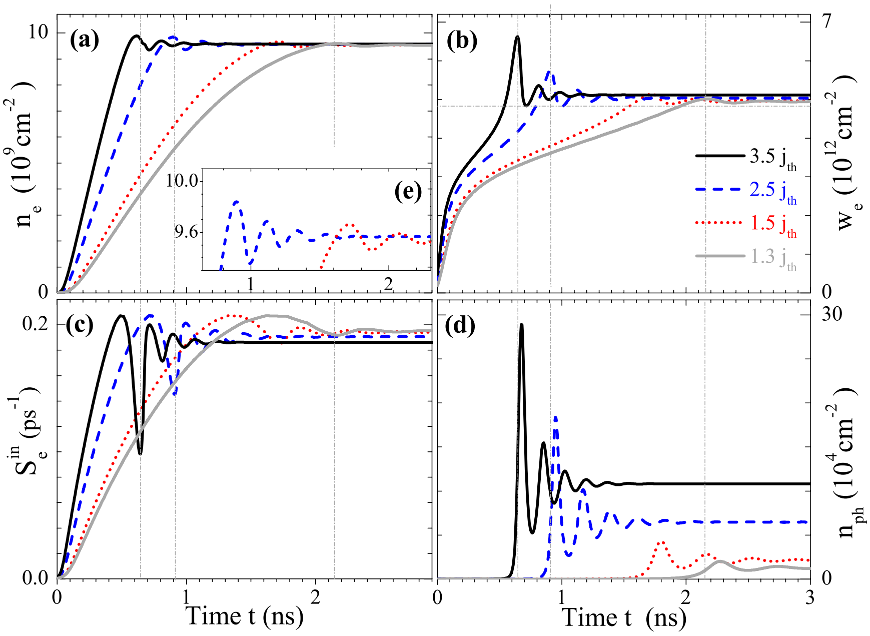

FIG. 9. (Color online) Turn-on dynamics in the weak damping regime for four different pump currents $1.3j_{\text{th}} \leq j \leq 3.5j_{\text{th}}$: (a) QD electron density n_e (inset (e) shows an enlargement), (b) WL electron density w_e, (c) scattering rate for electron in-scattering S_e^{in}, and (d) photon density n_{ph}. Parameters as in Fig. 8, but with different confinement factor $\Gamma=0.0015$.

densities strongly modulated around the saturation inversion on the other hand, as found in conventional semiconductor injection lasers. In the first case the set of parameters is identical to the one discussed above, while the second parameter set has a slightly increased optical confinement parameter $\Gamma=0.0015$. A phase portrait of the turn-on dynamics together with the steady state (fixed points) for different pump currents in the two-dimensional subspace (n_{ph}, n_e) is plotted in Fig. 7 for both parameter sets. The main figure indicates each steady state of the laser emission for pump currents $0 < j < 4j_{\text{th}}$ by a symbol. Black dots refer to $\Gamma=0.0011$ (strongly damped behavior), whereas blue stars correspond to $\Gamma=0.0015$ (weakly damped case). One difference between the two curves is the higher asymptotic steady state electron density $n_e(t\rightarrow\infty)$ for the strongly damped case. Here nearly all QDs are filled with an electron leading to a steady-state electron density of $n_e(t\rightarrow\infty)\approx N^{\text{QD}}$. It is also obvious that the steady-state electron density decreases slightly with increasing pump current which indicates depletion of the inversion saturation. For $\Gamma=0.0015$, on the other hand, $n_e(t\rightarrow\infty)$ stays approximately constant with increasing j, as in conventional lasers.

In addition to the steady states, the inset of Fig. 7 contains selected trajectories for both parameter sets as a blow-up of electron densities near the lasing threshold. It can easily be seen that the two trajectories resulting from the system with $\Gamma=0.0015$ show the conventional spiral form with an anticlockwise rotation, while the trajectories representing the strongly damped case have a more complex form. With the turn-on of the laser the electron density decreases. Later it starts to increase again while the photon density is still rising a little, resulting in a clockwise rotation of the spiral. We stress that in the strongly damped case the self-consistently obtained ratio between w_e and w_h, i.e., the factor g_c, depends strongly on the pump current as soon as the laser operation is in the damped limit, i.e., the scattering processes are dominant [see Fig. 11(a)].

The complex behavior of the QD laser dynamics is a result of the strongly nonlinear scattering rates $S_b^{\text{in/out}}$ and can be explained by analyzing their time evolution. This is done

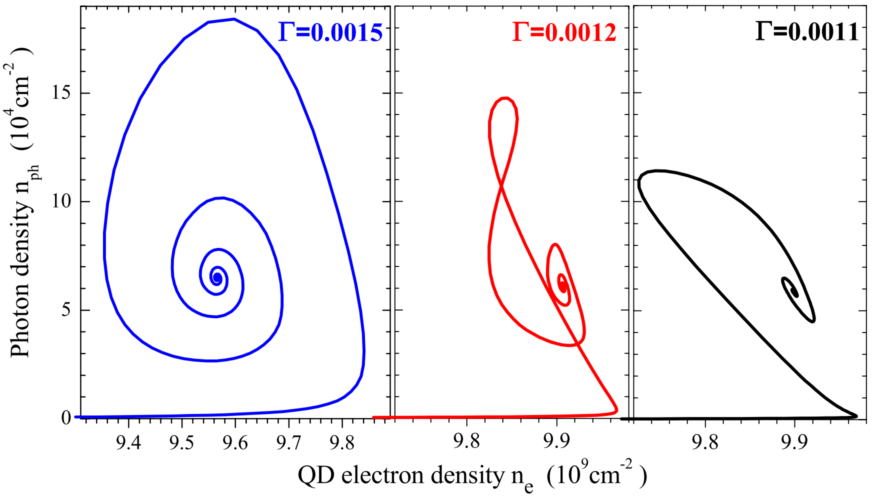

FIG. 10. (Color online) Phase portrait of turn-on dynamics for three different confinement factors and a pump current of $j=2.5j_{\text{th}}$, $g_c=2.5$: (a) weakly damped relaxation oscillations with $\Gamma=0.0015$, (b) crossover regime with $\Gamma=0.0012$ and (c) strongly damped dynamics with $\Gamma=0.0011$

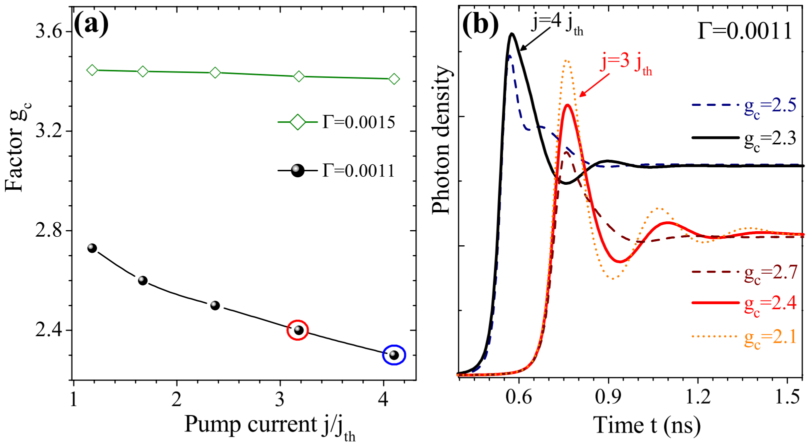

FIG. 11. (Color online) (a) WL hole-electron density ratio $g_c = w_h/w_e$ in dependence of the pump current j; green diamonds and black dots correspond to $\Gamma = 0.0015$ and $\Gamma = 0.0011$, respectively, (b) turn-on dynamics of the QD laser ($\Gamma = 0.0011$) calculated for different values of g_c and two different pump currents (black: $4j_{\mathrm{th}}$, red: $3j_{\mathrm{th}}$). The solid lines correspond to the correct self-consistent value of g_c.

in Figs. 8 and 9 for $\Gamma = 0.0011$ and $\Gamma = 0.0015$, respectively. Both figures show $n_e(t)$, $w_e(t)$, $S_e^{\mathrm{in}}(t)$, and $n_{\mathrm{ph}}(t)$ for various pump currents in the range of $1.3j_{\mathrm{th}}$ to $4j_{\mathrm{th}}$. The relaxation oscillations of $n_{\mathrm{ph}}(t)$ shown in Figs. 8(d) and 9(d) were already discussed above. It should be noted that for larger Γ their frequency is changed to a higher value as indicated in Fig. 6(a) (open diamonds). Due to the low damping, the first peak is much higher and its full width at half maximum is smaller [see Fig. 6(b)]. The differences in the turn-on behavior can be traced back to the scattering rates, especially to $S_e^{\mathrm{in}}(t)$. As depicted in Fig. 2(a), it shows a pronounced maximum at $w_e = 5 \times 10^{12}\ \mathrm{cm}^{-2}$. Thus, for higher w_e the in-scattering into the QDs is rapidly reduced resulting in a lower electron density in the QDs and therefore an even higher electron density in the WL ($w_e(t \to \infty)$). In the weakly damped case the observed WL densities are always located around the maximum value of $S_e^{\mathrm{in}}(t)$ while for the strongly damped case w_e is much higher so that the values of $S_e^{\mathrm{in}}(t)$ sharply decrease [Fig. 8(c)]. As a result the electron density n_e in the QDs is higher and close to N^{QD} in the strongly damped case [compare insets of Figs. 8(a) and 9(a)]. In the weakly damped case the QDs are not completely filled; thus in-scattering is still possible leading to a smaller WL electron density w_e [compare Figs. 8(b) and 9(b)] and to a stronger modulation of the QD electron density and of the gain with time [inset of Fig. 9(a)], which results in pronounced relaxation oscillations.

In between those two regimes a crossover between the different dynamic behavior is found. This is evident in the phase portraits shown in Fig. 10. The confinement parameter is changed between $\Gamma = 0.0015$ and $\Gamma = 0.0011$. It can be nicely seen that in between the strongly oscillating regime and the strongly damped case a cleflike form of the trajectory in the phase space is found [Fig. 10(b)]. Thus the turn-on dynamics is continuously transformed from the clockwise rotation in the (n_{ph}, n_e) plane into the anticlockwise rotation, whereby the amplitude modulation is reduced indicating stronger damping of the relaxation oscillations. For quantum well lasers larger confinement factors Γ are expected, since the optical confinement is governed by the vertical contribution Γ_z only.

The ratio of WL hole and electron densities g_c depends strongly on the pump current as soon as the laser is operated in the strongly damped limit ($\Gamma = 0.0011$), i.e., the scattering processes are dominant [see Fig. 11(a)]. Figure 11(b) exemplarily shows the effect of a wrong choice of g_c upon the turn-on dynamics in that regime. If g_c is chosen too large [dashed lines in Fig. 11(b)], there are distinct artifacts in the simulations, where the width and height of the first relaxation oscillation peak shrinks while a second maximum appears in the transient. An underestimated g_c has a smaller effect on the dynamics [red dotted line in Fig. 11(b)]. However, it changes f_{RO} to higher values and evokes more pronounced relaxation oscillations. Note that in the weak damping regime ($\Gamma = 0.0015$) where we find strong relaxation oscillations, g_c is constant up to less than one percent [see open diamonds in Fig. 11(a)]. According to the arguments given above this is expected as in this regime the radiative processes are more important.

VI. MODULATION RESPONSE

In this section we analyze the simulated small- and large-signal modulation responses of the laser in comparison with experimental observations. The large-signal behavior of a la-

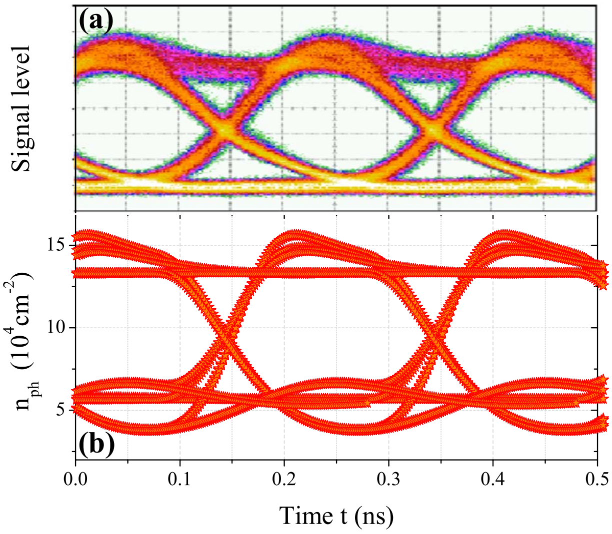

FIG. 12. (Color online) (a) Measured and (b) simulated eye pattern diagram of the QD laser. Simulation parameters as in Fig. 3. The high and low current-level of the 5 Gbit/s (200ps period) pump current are chosen as $j = 4.5j_{\mathrm{th}}$ and $j = 2.5j_{\mathrm{th}}$, respectively.

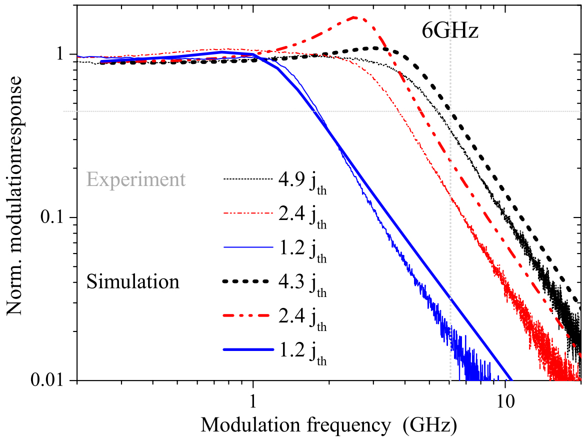

FIG. 13. (Color online) Modulation response of the QD laser for three different pump currents $j=1.2j_{\mathrm{th}}\ldots4.9j_{\mathrm{th}}$ for measured (thin lines) and simulated (thick lines) data. Parameters as in Fig. 3.

TABLE II. Scattering rates and scattering times evaluated at the steady state for different pump currents j.

$j\rightarrow$	$1.6j_{\mathrm{th}}$	$2.1j_{\mathrm{th}}$	$2.7j_{\mathrm{th}}$	$3.9j_{\mathrm{th}}$
Rate (ps^{-1})				
S_e^{in}	0.196	0.199	0.178	0.185
S_e^{out}	$8.3\cdot10^{-5}$	$4.9\cdot10^{-5}$	$2.0\cdot10^{-5}$	$0.6\cdot10^{-5}$
S_h^{in}	0.0402	0.0401	0.040	0.039
S_h^{out}	0.0525	0.0506	0.0484	0.0443
Time (ps)				
τ_e	5.1	5.02	5.62	5.4
τ_h	10.8	11.0	11.3	12.0

ser diode determines its capability for digital data transfer. In order to evaluate the large-signal behavior, so-called eye pattern diagrams are measured by pumping the laser with a random bit sequence, as shown in Fig. 5(b). This signal enters the diode and is converted to a stream of optical data. The *opening* of the eye pattern is the essential quality parameter. The low current is chosen above threshold so that the laser does not turn off and possibly create another turn-on delay. Typical for the QD laser is the advantageous symmetric shape of the eye patterns that result from the strong damping. As can be seen from Fig. 12, the simulated eye pattern for a transmission rate of 5 Gbit/s shows very good agreement with the measured one if eye-*openness*, symmetry, and high level overshoot are compared. The simulated undershoot of the low level, however, shows small discrepancies with the experiment that still need to be understood.

The small-signal response of a laser is measured by superimposing a small modulated signal with frequencies between 0.2 and 20 GHz upon the stationary pump current j. The modulation amplitude is a small fraction (1 percent) of the pump current. As a result the steady-state laser output becomes periodically modulated. The measured and simulated small-signal response is shown in Fig. 13 for various pump currents j. For larger j the cut-off frequency is shifted to higher values. Our model describes the modulation response for a wide range of operating conditions, and thus opens up the possibility to predict trends and optimize parameters for realistic applications in data transmission.

VII. CONCLUSION

The strongly damped relaxation oscillations of quantum dot lasers have been quantitatively explained by a novel mechanism which is markedly distinct from conventional lasers and involves strongly nonlinear carrier-carrier scattering from the wetting layer into quantum dot states. We have shown by a microscopically based five-variable rate equation model that conventional weakly damped anticlockwise relaxation oscillations on one hand, and strongly damped anomalous relaxation oscillations on the other hand, correspond to two different nonlinear dynamic regimes. In our simulations a transition between these two regimes can be obtained by choosing different values of the optical confinement factor.

Furthermore we have demonstrated the importance of the mixed electron-hole Auger capture processes that depend on both the electron and the hole density in the wetting layer, thereby improving our previous results which considerably overestimated the relaxation oscillation frequency. Only if the different concentrations of electrons and holes in the wetting layer and the dependence of their ratio upon the pump current are taken into account, substantial discrepancies with experiment regarding the shape and the frequency of the relaxation oscillations can be avoided. The turn-on dynamics and both the large- and small-signal modulation response have been analyzed for a variety of parameters over a wide range of different pump currents in excellent agreement with experiment.

ACKNOWLEDGMENTS

This work was performed in the framework of Sfb 787. E.M. is grateful to Studienstiftung des deutschen Volkes for financial support. We thank G. Fiol for stimulating discussions.

APPENDIX

In order to enable a comparison with simplified models this Appendix provides fitting functions for the numerically calculated scattering rates. To obtain correct results, the variables w_e and w_h have to be inserted in units of $10^{11}\ \mathrm{cm}^{-2}$. It has to be noted that these fits have to be used with great care since the dynamic response depends sensitively on the nonlinear scattering rates,

$$\begin{aligned}
S_e^{\text{in}}(w_e) &= F\left(\frac{1}{1+e^{(38-w_e)/5.4}}\right)\left(\frac{e^{(38-w_e)/B}}{1+e^{(38-w_e)/B}}\right)+A\cdot e^{-2(w_e\,-\,124.5)^2/29.6^2}\\
F &= 0.715+0.6g_c-0.19g_c^2\\
B &= -6.9+40.5g_c-11g_c^2\\
A &= 0.0116
\end{aligned}$$

$$\begin{aligned}
S_h^{\text{in}}(w_h) &= \tanh(B\cdot w_h)\frac{A}{C\sqrt{\pi/2}}e^{-2(w_h\,-\,182)^2/C^2},\\
A &= 8+0.228g_c,\\
B &= 0.096-0.0095g_c\\
C &= 171
\end{aligned}$$

$$\begin{aligned}
S_h^{\text{out}}(w_h) &= F(1-e^{-(w_h-1.2)/1.7})^{0.7}e^{-(w_h)^2/18854}+e^{-(w_h-D)/26.4}\\
F &= 0.2823+0.0201g_c\\
D &= -0.9-3g_c
\end{aligned}$$

$$\begin{aligned}
S_e^{\text{out}}(w_e) &= (1-e^{(1-w_e)/2})^{0.9}e^{-(w_e)^2/B}+e^{(1.73-w_e)/C}+A\cdot e^{-\,(w_e\,-\,27.5)^2/137.8}\\
B &= 963-153g_c\\
C &= 12.4-5.35g_c+0.718g_c^2\\
A &= 0.1154.
\end{aligned}$$

Table II gives the scattering rates S_e^{in}, S_e^{out}, S_h^{in}, S_h^{out} and scattering times τ_e and τ_h evaluated at the steady state for different pump currents j, which might be useful for a small-signal analysis around the steady state.

---

[1] D. Bimberg, M. Grundmann, and N. N. Ledentsov, *Quantum Dot Heterostructures* (Wiley, New York, 1999).

[2] D. Bimberg, M. Kuntz, and M. Lämmlin, Appl. Phys. A **80**, 1179 (2005).

[3] D. Bimberg, Electron. Lett. **44**, 168 (2008).

[4] H. Huang and D. G. Deppe, IEEE J. Quantum Electron. **37**, 691 (2001).

[5] G. Huyet, D. O'Brien, S. P. Hegarty, J. G. McInerney, A. V. Uskov, D. Bimberg, C. Ribbat, V. M. Ustinov, A. E. Zhukov, S. S. Mikhrin, A. R. Kosvh, J. K. White, K. Hinzer, and A. J. SpringThorpe, Phys. Status Solidi B **201**, 345 (2004).

[6] D. O'Brien, S. P. Hegarty, G. Huyet, and A. V. Uskov, Opt. Lett. **29**, 1072 (2004).

[7] A. Markus and A. Fiore, Phys. Status Solidi A **201**, 338 (2004).

[8] H. Dery and G. Eisenstein, IEEE J. Quantum Electron. **41**, 26 (2005).

[9] C. Xing and E. A. Avrutin, J. Appl. Phys. **97**, 104301 (2005).

[10] A. E. Viktorov, P. Mandel, A. G. Vladimirov, and U. Bandelow, Appl. Phys. Lett. **88**, 201102 (2006).

[11] A. Fiore and A. Markus, IEEE J. Quantum Electron. **43**, 287 (2007).

[12] T. Erneux, E. A. Viktorov, and P. Mandel, Phys. Rev. A **76**, 023819 (2007).

[13] E. Schöll, D. Bimberg, H. Schumacher, and P. T. Landsberg, IEEE J. Quantum Electron. **20**, 394 (1984).

[14] D. Bimberg, K. Ketterer, E. H. Böttcher, and E. Schöll, Int. J. Electron. **60**, 23 (1986).

[15] M. Grundmann, Appl. Phys. Lett. **77**, 4265 (2000).

[16] M. Grundmann, Appl. Phys. Lett. **77**, 1428 (2000).

[17] E. Gehrig and O. Hess, Phys. Rev. A **65**, 033804 (2002).

[18] M. Lorke, F. Jahnke, and W. W. Chow, Appl. Phys. Lett. **90**, 051112 (2007).

[19] W. W. Chow and S. W. Koch, *Semiconductor-Laser Fundamentals* (Springer, Berlin, 2004).

[20] W. W. Chow and S. W. Koch, IEEE J. Quantum Electron. **41**, 495 (2005).

[21] C. Gies, J. Wiersig, M. Lorke, and F. Jahnke, Phys. Rev. A **75**, 013803 (2007).

[22] E. Malić, K. J. Ahn, M. J. P. Bormann, P. Hövel, E. Schöll, A. Knorr, M. Kuntz, and D. Bimberg, Appl. Phys. Lett. **89**, 101107 (2006).

[23] E. Malić, M. J. P. Bormann, P. Hövel, M. Kuntz, D. Bimberg, A. Knorr, and E. Schöll, IEEE J. Sel. Top. Quantum Electron. **13**, 1242 (2007).

[24] R. Wetzler, A. Wacker, and E. Schöll, J. Appl. Phys. **95**, 7966 (2004).

[25] T. R. Nielsen, P. Gartner, and F. Jahnke, Phys. Rev. B **69**, 235314 (2004).

[26] E. Schöll, IEEE J. Quantum Electron. **24**, 435 (1988).

[27] M. Kuntz, Ph.D. thesis, Technische Universität Berlin, 2006.

[28] A. V. Uskov, F. Adler, H. Schweizer, and M. H. Pilkuhn, J. Appl. Phys. **81**, 7895 (1997).

[29] A. V. Uskov, Y. Boucher, J. L. Bihan, and J. McInerney, Appl. Phys. Lett. **73**, 1499 (1998).

[30] R. Wetzler, A. Wacker, and E. Schöll, Semicond. Sci. Technol. **19**, S43 (2004).

[31] M. Lorke, T. R. Nielsen, J. Seebeck, P. Gartner, and F. Jahnke, Phys. Rev. B **73**, 085324 (2006).

[32] T. Piwonski, I. O'Driscoll, J. Houlihan, G. Huyet, R. J. Manning, and A. V. Uskov, Appl. Phys. Lett. **90**, 122108 (2007).

[33] M. Lindberg and S. W. Koch, Phys. Rev. B **38**, 3342 (1988).

[34] F. Rossi and T. Kuhn, Rev. Mod. Phys. **74**, 895 (2002).

[35] P. T. Landsberg, *Recombination in Semiconductors* (Cambridge University Press, Cambridge, 1991).

[36] Scattering rates were calculated with $m_e = 0.043 m_0$, $m_h = 0.45 m_0$, and $\varepsilon = 14.2$ which are averaged values of InAs and GaAs. $L_{\mathrm{eff}} = 8\ \mathrm{nm}$, $E_e(T = 300\ \mathrm{K}) = 195\ \mathrm{meV}$, $E_h(T = 300\ \mathrm{K}) = 105\ \mathrm{meV}$.